Retrieval of Solar-induced Chlorophyll Fluorescence from Satellite Measurements: Comparison of SIF between TanSat and OCO-2

Lu Yao[1, 2], Yi Liu[1,3], Dongxu Yang[1,3], Zhaonan Cai[1], Jing Wang[1], Chao Lin[4], Naimeng Lu[5], Daren Lyu[1], Longfei Tian[6], Maohua Wang[3], Zengshan Yin[6], Yuquan Zheng[4], Sisi Wang[7]

[1]Key Laboratory of Middle Atmosphere and Global Environment Observation, Institute of Atmospheric Physics, Chinese Academy of Sciences, No. 40, Huayan Li, Chaoyang District, Beijing 100029, China
[2]University of Chinese Academy of Sciences, No. 19A, Yuquan Lu, Shijing Shan District, Beijing 100049, China
[3]Shanghai Advanced Research Institute, Chinese Academy of Sciences, Shanghai 201210, China
[4]Changchun Institute of Optics, Fine Mechanics and Physics, Changchun 130033, China
[5]National Satellite Meteorological Center, China Meteorological Administration, Beijing 100081, China
[6]Shanghai Engineering Center for Microsatellites, Shanghai 201203, China
[7]National Remote Sensing Center of China, Beijing 100036, China

Correspondence to: Dongxu Yang (yangdx@mail.iap.ac.cn)

Abstract. Solar-induced chlorophyll fluorescence (SIF) is emitted during photosynthesis in plant leaves. It constitutes a small additional offset to reflected radiance and can be observed by sensitive instruments that with high SNR and spectral resolution. The Chinese global carbon dioxide monitoring satellite (TanSat), as its mission, acquires greenhouse gas column density. The advanced technical characteristics of the hyper-spectrum grating spectrometer (ACGS) onboard TanSat enable SIF retrieval from space observations in the O_2-A band. In this study, one-year SIF data at sounding scale was processed globally from Orbiting Carbon Observatory-2 (OCO-2) and TanSat using a physical-based algorithm. A comparison between the SIF results retrieved from OCO-2 spectra and the official OCO-2 SIF product (OCO2_Level 2_Lite_SIF.8r) shows their strong linear relationship ($R^2 > 0.85$) and suggests the reliability of the SIF retrieval algorithm. The global distribution showed that the SIF retrieved from the two satellites shared the same spatial pattern for all seasons with the gridded SIF difference less than 0.3 W m^{-2} μm^{-1} sr^{-1}, and they also agreed well with the official OCO-2 SIF product with the difference less than 0.2 W m^{-2} μm^{-1} sr^{-1}. The retrieval uncertainty of seasonal-gridded TanSat SIF is less than 0.03 W m^{-2} μm^{-1} sr^{-1} whereas the uncertainty of each sounding ranges from 0.1 to 0.6 W m^{-2} μm^{-1} sr^{-1}. The relationship between annual averaged SIF products and FLUXCOM gross primary productivity (GPP) was also estimated for six vegetation types in a 1° × 1° grid over the globe, indicating that the SIF data from the two satellites have the same potential in quantitatively characterizing ecosystem productivity. The spatiotemporal consistency between TanSat and OCO-2 and their comparable data quality make the comprehensive usage of the two mission products possible. Data supplemented by TanSat observations are expected to contribute to the development of global SIF maps with more spatiotemporal detail, which will advance global research on vegetation photosynthesis.

1 Introduction

Terrestrial vegetation accounts for a large part of the ecosystem, with its photosynthesis and respiration processes playing important roles in the global carbon cycle. Incoming radiation is absorbed, reflected, and/or transmitted by plant leaves. A portion of the absorbed radiation is used by the chlorophyll in plant leaves for carbon fixation, while the rest is either dissipated as heat or re-emitted as solar-induced chlorophyll fluorescence (SIF) at longer wavelengths (Frankenberg et al., 2011a, 2014). In contrast to the traditional remotely sensed vegetation indices obtained from some studies (Frankenberg et al., 2011b; Guanter et al., 2014; Li et al., 2018; Sun et al., 2017a; Yang et al., 2015; Zhang et al., 2014), SIF offers the potential to measure photosynthesis activity and gross primary production (GPP), due to the strong correlation between these measures (Frankenberg et al., 2011b; Guanter et al., 2012, 2014). The fluorescence emission (Fs) adds a low-intensity radiance less than $10\ \mathrm{W\ m^{-2}\ \mu m^{-1}\ sr^{-1}}$ and fills in the solar absorption features of the reflected spectrum (Frankenberg et al., 2011a). The filling-in effect of the solar lines (Fraunhofer lines) is the basic principle applied to measure SIF from space using the capabilities of hyperspectral observation (Frankenberg et al., 2011b; Guanter et al., 2012).

The first attempt at SIF research based on space-based observations was performed using images acquired by the Medium Resolution Imaging Spectrometer (MERIS) onboard the ENVIronmental SATellite (ENVISAT) (Guanter et al., 2007). This led to a new idea for conducting SIF studies on a global scale. The first global SIF map was retrieved with high-resolution spectra from the Greenhouse-gases Observing SATellite (GOSAT) (Joiner et al., 2011; Frankenberg et al., 2011b). After that, SIF retrievals were implemented from a variety of satellite measurements, such as those from the Global Ozone Monitoring Experiment-2 (GOME-2) instruments onboard meteorological operational satellites, SCIAMACHY on board ENVISAT, and Orbiting Carbon Observatory-2 (OCO-2) (Joiner et al., 2016; Köhler et al., 2015). The TROPOspheric Monitoring Instrument (TROPOMI) on board Sentinel 5 Precursor (S-5P) provides more efficient SIF observations in terms of global coverage and new opportunities for exploring the application potential of SIF data in the terrestrial biosphere as well as in climate research (Doughty et al., 2019; Köhler et al., 2018b). Furthermore, an upcoming European Space Agency mission called FLuorescence EXplorer (FLEX), the first satellite dedicated to SIF emission observation, will launch in the middle of 2024 (Drusch et al., 2017). Many studies on SIF applications have been initiated with the accumulation of SIF products in recent years. The responses of satellite-measured SIF to environmental conditions have been applied to drought dynamics monitoring and regional vegetation water stress estimation (Lee et al., 2013; Sun et al., 2015; Yoshida et al., 2015). As a proxy of photosynthesis, SIF acts as a powerful constraint parameter in estimating carbon exchange in an ecosystem between the atmosphere, ocean, and soil; as such, the analysis of the relationship between SIF and GPP has become an important research topic (Li et al., 2018; Köhler et al., 2018a; Sun et al., 2017a; Zhang et al., 2018). The strong linear relationship between them paves the way for improving terrestrial ecosystem model simulation of GPP, along with consequent improvement of global carbon flux estimation (MacBean et al., 2018; Yin et al., 2020). GPP estimations based on satellite-measured SIF have proven to be an effective method validated by in-situ flux observations (Joiner et al., 2018; Qiu et al., 2020). However, uncertainty in the factors that determine the relationship between SIF and GPP still exists and is a key

68 limitation in the application of SIF to flux estimation. Based on multi-satellite SIF products, eddy covariance flux tower
69 observations, and ecological models, the relationship between SIF and GPP under different environmental conditions has
70 been discussed in a number of studies to analyze the dominant factors for the growing status of different biomes, such as
71 temperature, soil moisture, and vegetation types (Chen et al., 2020; Doughty et al., 2019; Li et al., 2020; Qiu et al., 2020; Yin
72 et al., 2020).

73 The Chinese global carbon dioxide monitoring satellite (TanSat) was launched in December 2016. Aiming at acquiring CO_2
74 concentrations as OCO-2, TanSat flies in a sun-synchronous orbit at approximately 700 km in height with a 16-day repeat
75 cycle and an equator crossing time of ~1:30 p.m. local time (Cai et al., 2014; Liu et al., 2018; Yang et al., 2018). Onboard
76 TanSat, the hyperspectral Atmospheric Carbon-dioxide Grating Spectrometer (ACGS) is designed to separately record solar
77 backscatter spectra in three channels centered at 0.76 μm (O_2-A band), 1.61 μm (weak CO_2 absorption band), and 2.06 μm
78 (strong CO_2 absorption band). With the recorded spectra, many Optimal Estimation Method (OEM) full physics retrieval
79 algorithms have been developed and applied for XCO_2 retrievals (Boesche et al., 2009; Butz et al., 2009, 2011; O'Dell et al.,
80 2012; Reuter et al., 2010; Yang et al., 2015b; Yoshida et al., 2011, 2013). The Institute of Atmospheric Physics Carbon
81 Dioxide Retrieval Algorithm for Satellite Remote Sensing (IAPCAS) algorithm has been applied for TanSat retrieval (Yang
82 et al., 2018; Yang et al., 2021) and was also previously tested on GOSAT and OCO-2 missions (Yang et al., 2015b).
83 However, the fluorescence feature causes substantial biases when retrieving surface pressure and scattering parameters from
84 the O_2-A band, and the associated errors propagate into the XCO_2 retrievals. In previous XCO_2 retrieval, the surface
85 emissions were well modeled as a continuum zero offset of the O_2-A band to reduce errors (Frankenberg et al., 2011a, 2012;
86 Butz et al., 2009, 2010; Joiner et al., 2012). The high spectral resolution of ~0.044 nm and a signal-to-noise ratio of ~360 in
87 the O_2-A band makes it possible to obtain SIF from space measurements, with a spatial resolution of 2 km × 2 km in nadir
88 mode (Liu et al., 2018).

89 Various approaches have been used to infer SIF from satellite measurements (Frankenberg et al., 2011b, 2014a, 2014b;
90 Guanter et al., 2007, 2012, 2015; Joiner et al., 2011, 2013, 2016; Köhler et al., 2015, 2018b). The SIF signal induces a
91 filling-in effect of solar lines, which can be used for SIF retrieval, as the fractional depth of solar Fraunhofer lines does not
92 change during radiation transmission in the atmosphere. To recognize the filling-in features by SIF, high-resolution spectra
93 and an instrument spectral response function (ISRF) are required to describe subtle changes in the spectral absorption lines.
94 With the detailed spectral features, a method was developed based on solar line fitting and the Beer-Lambertian law. This
95 method is robust and accurate when the spectrum is out of the influence of telluric absorptions, even in the presence of
96 aerosols (Frankenberg et al., 2011a; Joiner et al., 2011); in the current study, this method was applied to develop the
97 IAPCAS/SIF algorithm. Another SIF retrieval method is the data-driven algorithm based on the singular value
98 decomposition (SVD) technique (Joiner et al., 2011; Guanter et al., 2012), which has been broadly applied in GOSAT, OCO-
99 2, TanSat and TROPOMI SIF retrieval (Joiner et al., 2011; Guanter et al., 2012, 2015; Frankenberg et al., 2014a; Du et al.,
100 2018; Köhler et al., 2018b). In the data-driven method, the spectrum is represented as a linear combination of the SIF signal
101 and several singular vectors that are trained from non-fluorescent scenes by SVD; thus, the SIF signal can be obtained with

102 linear least-squares fitting (Du et al., 2018; Guanter et al., 2012). The first TanSat SIF map was obtained by the SVD
103 method (Du et al., 2018), in a previous study, a preliminary comparison between the TanSat SIF products retrieved by
104 IAPCAS/SIF algorithm and the SVD data-driven method was performed, and the comparison shows that the two SIF
105 products share a similar global pattern and signal magnitude for all seasons while different biases still exist in four seasons
106 (Yao et al., 2021). The different biases in four seasons may be caused by the different training samples of the SVD method.
107 In order to obtain stable SIF data products from TanSat and other subsequent satellite missions, it is particularly important to
108 establish a stable and high-precision SIF inversion algorithm. To validate the IAPCAS/SIF algorithm and test the potential of
109 comprehensive usage of multi-satellites SIF data in analysis, in this study, we detailed the TanSat SIF retrieval using the
110 IAPCAS/SIF algorithm and made the comparison of SIF products between TanSat and OCO-2.

111 **2 Data and retrieval algorithm**

112 **2.1 Retrieval Principle and Method**

113 We used TanSat version 2 Level 1B (L1B) nadir-mode earth observation data in the retrieval process. The measurements
114 covered the period from March 2017 to February 2018. Polarized radiance in the O_2-A band with a spectral resolution of
115 0.044 nm was provided in the L1B data, and two micro-windows near 757 nm (758.3-759.2 nm) and 771 nm (769.6-770.3
116 nm) were chosen to retrieve the top-of-atmosphere (TOA) SIF while avoiding the contamination from strong lines of
117 atmospheric gas absorption. The retrieval was independent for each micro-window as shown in Figure 1. To avoid
118 duplication of information, we use the SIF product at 757 nm as the example in the analysis.
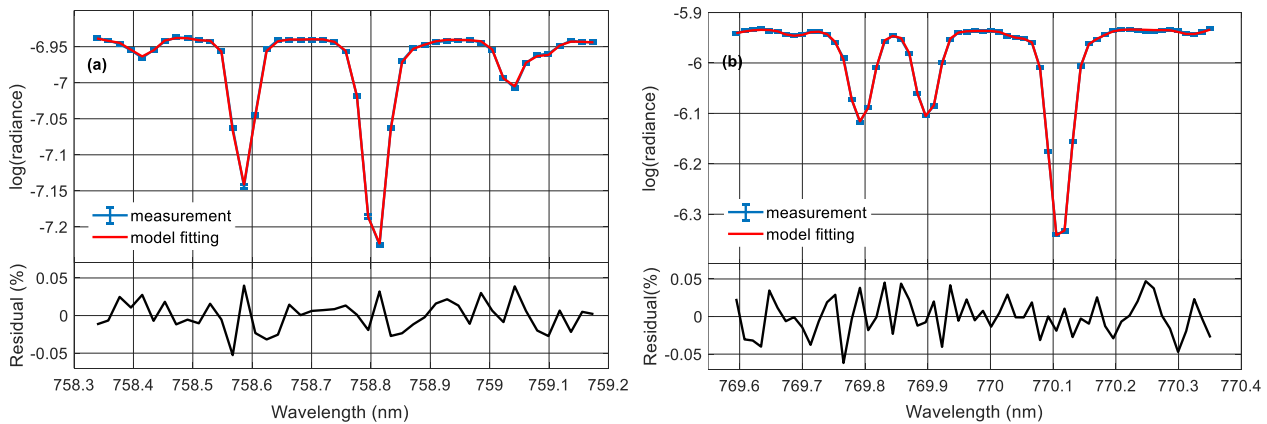
119

120 **Figure 1: The fitted spectra and residuals for the (a) 757 nm and (b) 771 nm micro-windows of TanSat measurement. The error**
121 **bar of the measured spectra depicts the estimated precision of each TanSat sounding.**

122

123 Filling-in on solar lines by chlorophyll fluorescence in the O_2-A band can be detected in the hyperspectral measurements
124 from TanSat. This effect on spectral radiance is different from the impact of atmospheric and surface processes, e.g.,

125 scattering and absorption. For example, scattering by aerosols and clouds does not change the relative depth of clear solar

126 lines, unlike the SIF emission signal. We applied the differential optical absorption spectroscopy (DOAS) technique to

127 IAPCAS/SIF algorithm for TanSat measurement (Frankenberg, 2014b; Sun et al., 2018).

128 The TOA spectral radiance (L_{TOA}^{λ}) at wavelength λ can be represented as follows:

129 $$L_{TOA}^{\lambda} = I_t^{\lambda} \cdot \mu_0 \cdot (\rho_0^{\lambda} + \frac{\rho_s^{\lambda} \cdot T_{\downarrow}^{\lambda} \cdot T_{\uparrow}^{\lambda}}{\pi}) + F_{TOA}^{\lambda} \tag{1}$$

130 where I_t^{λ} is the incident solar irradiance at the TOA, μ_0 is the cosine of the solar zenith angle (SZA), ρ_0^{λ} is atmospheric path

131 reflectance, ρ_s^{λ} is surface reflectance, and $T_{\downarrow}^{\lambda}$ and $T_{\uparrow}^{\lambda}$ are the total atmospheric transmittances along the light-path in the

132 downstream and upstream directions, respectively. F_{TOA}^{λ} is the SIF radiance at TOA.

133 The first term on the right of Eq. (1) represents the transmission process of solar radiance. In the micro-windows used in SIF

134 retrieval, gas absorption is very weak and smooth, and hence, the atmosphere term $\mu_0 \cdot (\rho_0^{\lambda} + \frac{\rho_s^{\lambda} \cdot T_{\downarrow}^{\lambda} \cdot T_{\uparrow}^{\lambda}}{\pi})$ can be simplified to a

135 low-order polynomial that varies with λ (Joiner et al., 2013; Sun et al., 2018); this is always valid as long as the spectrum

136 fitting range is out of sharp atmospheric absorptions. In the retrieval, the spectral radiance measurement was converted to

137 logarithmic space by the instrument and the radiative transfer process $f(F_s^{rel}, \boldsymbol{a})$ was represented as follows:

138 $$f(F_s^{rel}, \boldsymbol{a}) = log(< I_t + F_s^{rel} >) + \sum_{i=0}^{n} a_i \cdot \lambda^i \tag{2}$$

139 where $< >$ denote the convolution with the ISRF from line-by-line spectra. The polynomial coefficient $\boldsymbol{a}$ determines the

140 wavelength dependence polynomial for the atmosphere term; in the retrieval, we used a second-order polynomial ($n = 2$).

141 The radiance is normalized to the continuum level; hence, I_t is a normalized disk-integrated solar transmission model, and

142 F_s^{rel} is the normalized relative SIF. In the micro-window, SIF was regarded as a constant signal due to its small changes.

143 Although the atmospheric gas absorption was very weak in the micro-window, the weak absorption and the far-wing effects

144 (O_2 lines) can still change spectral features, which induces errors in spectrum fitting. Therefore, we used the European

145 Centre for Medium-Range Weather Forecasts (ECMWF) interim surface pressure ($0.75° \times 0.75°$) to estimate O_2 absorption

146 firstly and then modified the absorption feature by a scale factor. The scale factor is obtained simultaneously in SIF retrieval

147 to reduce the error induced by the uncertainty in surface pressure. As described by Yang (2020), there is also a continuum

148 feature in TanSat L1B data that needs to be considered for the high-quality fitting of the O_2-A band. However, in this study,

149 this continuum feature was not corrected, as the impact of such a smooth continuum variation in the micro-window is weak

150 and the polynomial continuum model is capable of compensating for most of this effect.

151 The state vector list in the retrieval includes the relative SIF signal F_s^{rel}, a wavenumber shift, the scale of O_2 column

152 absorption for surface pressure correction, and coefficients of the polynomial. The continuum level radiance I_{cont} within the

153 fitting window is calculated using the radiance outside the absorption features in the micro-window and is then used for the

154 actual SIF signal calculation thus: $F = F_s^{rel} \cdot I_{cont}$.

155 In the IAPCAS/SIF algorithm, we used an OEM for state vector optimization in the retrieval process. Unlike XCO2 retrieval,

156 SIF retrieval employs a state vector with fewer elements and a much simpler forward model, so there is no need to perform

157 complex radiation transmission calculations. Considering the low complexity of SIF retrieval, the Gauss-Newton method
158 was applied in inversion iteratively to find the optimal solution.

2.2 Bias Corrections

160 A systematic error remains in the raw SIF retrieval output if no bias correction is performed; similar results have been
161 reported in GOSAT and OCO-2 SIF retrieval studies (Frankenberg et al., 2011a, 2011b; Sun et al., 2018). This is because the
162 SIF signal is weak (e.g., typically ~1-2% of the continuum level radiance), which means that even a small issue in the
163 measurement, such as a zero-offset caused by radiometric calibration error, could induce significant bias. Unfortunately, the
164 lack of knowledge on in-flight instrument performance makes it difficult to perform a direct systematic bias correction in the
165 measured spectrum. In the retrieval, a continuum level radiance bin fit was used to estimate the bias. The bins have a
166 continuum level radiance interval of 5 W $m^{-2}\,\mu m^{-1}$ sr^{-1}. In each bin, the mean bias was estimated using all non-fluorescence
167 measurements, and a piecewise linear function was built from the mean bias of each continuum level radiance interval.
168 The non-fluorescence soundings that were used in the bias estimation were based on the dataset "sounding_landCover" in
169 TanSat L1B data. This dataset depends on the MODIS land cover product and provides a scheme consisting of 17 land cover
170 classifications defined by the International Geosphere-Biosphere Programme. These retrieved measurements marked as
171 "snow and ice," "barren," and "sparsely vegetated" were chosen to estimate the bias. Calibrations compensated for most of
172 the instrument degradations, but this alone was not perfect. To reduce the impact from the remaining minor discrepancies,
173 we built the bias correction function daily to obtain bias for each sounding via interpolation of the continuum level radiance
174 (Sun et al., 2017b, 2018).
175 The bias curves shown in Figure 2 differ significantly between TanSat and OCO-2. This is mostly due to the differences in
176 instrument performance and radiometric calibration. In general, the TanSat bias curves exhibited two peaks at radiance levels
177 of approximately 40 and 125 W $m^{-2}\,\mu m^{-1}$ sr^{-1}, separately, and most biases were larger than 0.015. For OCO-2, the curves
178 dropped sharply at low radiance levels, reaching the valley at a radiance level of approximately 40 W $m^{-2}\,\mu m^{-1}$ sr^{-1}, and then
179 increased slowly with the radiance level.

180
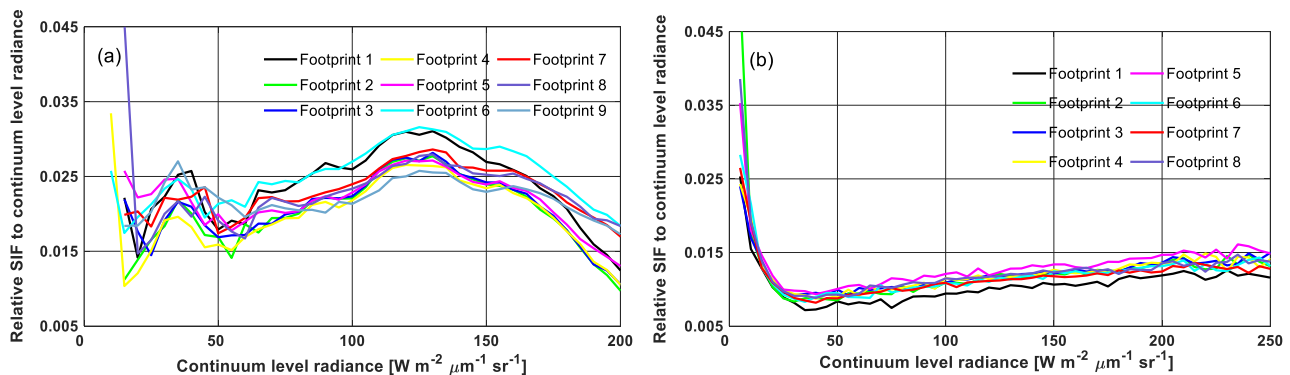
Figure 2: Variations in the bias correction curves of continuum level radiance from (a) TanSat on July 7, 2017, and (b) Orbiting Carbon Observatory-2 (OCO-2) on June 16, 2017. The different colors in the legend present different footprints of the satellite frame.

2.3 Data Quality Controls

Only data that passed quality control were used in further applications. There were two data quality control processes for the SIF products: pre-screening and post-screening. Pre-screening focused mainly on cloud screening; only cloud-free measurements were used in SIF retrieval. A surface pressure difference (SPD), defined as:

$$\Delta P_0 = |P_{retrieval} - P_{ECMWF}| \tag{3}$$

was used to evaluate cloud contamination along with a chi-square test

$$\chi^2 = \sum \frac{(y_{sim} - y_{obs})^2}{y_{noise}^2} \tag{4}$$

where y_{sim}, y_{obs}, and y_{noise} represent the model fitting spectrum, observation spectrum, and spectrum noise, respectively. $P_{retrieval}$ is the apparent surface pressure obtained from O_2-A band surface pressure retrieval, assuming a single scattering atmosphere. P_{ECMWF} is the ECMWF interim ($0.75° \times 0.75°$) surface pressure. A "cloud-free" measurement was required to simultaneously satisfy an SPD of less than 20 hPa and a χ^2 value of less than 80. Here, post-screening was applied to filter out "bad" retrievals; this screening process involved the following steps: (1) SIF retrievals with reduced χ^2 (χ_{red}^2) values ranging from 0.7 to 1.3 were considered "good" fitting, (2) continuum level radiance outside the range of $15 \sim 200$ W m^{-2} μm^{-1} sr^{-1} was screened out to avoid scenes too bright or too dark, and (3) soundings with the SZA higher than 60° were also filtered out.

2.4 IAPCAS versus IMAP-DOAS OCO-2 SIF Retrieval

Before applied to TanSat retrievals, we tested the IAPCAS/SIF algorithm on the OCO-2 L1B data first (OCO2_L1B_Science.8r) and then compared the retrieval results with the OCO-2 L2 Lite SIF product (OCO2_Level 2_Lite_SIF.8r) retrieved by the Iterative Maximum A Posteriori-Differential Optical Absorption Spectroscopy (IMAP-DOAS) algorithm (Frankenberg, 2014b). The Lite product provides the SIF value for each sounding on a daily basis and hence the SIF comparison could be performed on the sounding scale for each month.

Table 1 displays the relationship of OCO-2 SIF values between the IAPCAS/SIF and IMAP-DOAS at 757 nm micro-window for each month. Overall, the two SIF products were in good agreement. The linear fitting of the two SIF products suggests that they are highly correlated, as indicated by the strong linear relationship with R^2 mostly larger than 0.85 and the root mean square error (RMSE) of about 0.2 W m^{-2} μm^{-1} sr^{-1}. Good consistency between the two SIF products implies the reliability of the IAPCAS/SIF algorithm; thus, it was further applied to TanSat SIF retrieval. However, there was still a small bias in the comparisons, which was due, most likely, to the impact of differences in the bias correction method, retrieval algorithm, and fitting window.

Table 1: Summary of the relationship between the Institute of Atmospheric Physics Carbon Dioxide Retrieval Algorithm for Satellite Remote Sensing (IAPCAS) OCO-2 and Iterative Maximum A Posteriori-Differential Optical Absorption Spectroscopy (IMAP-DOAS) OCO-2 solar-induced chlorophyll fluorescence (SIF) products at 757nm micro-window.

month	Number of soundings	Slope	Intercept	R^2	RMSE/ W m^{-2} μm^{-1} sr^{-1}
2017/03	1097277	0.85	0.034	0.86	0.18
2017/04	1119464	0.86	0.045	0.87	0.19
2017/05	1054235	0.88	0.041	0.88	0.19
2017/06	1014848	0.91	0.032	0.90	0.19
2017/07	965309	0.92	0.011	0.91	0.19
2017/09	211219	0.88	0.005	0.81	0.23
2017/10	473359	0.88	0.031	0.88	0.17
2017/11	579009	0.87	0.022	0.85	0.19
2017/12	645134	0.87	0.020	0.88	0.16
2018/01	788655	0.87	0.019	0.88	0.17
2018/02*	629995	0.86	0.024	0.87	0.18

* Due to the lack of OCO-2 measurements in August 2017, the comparison is only performed for 11 months.

3 Results and Discussion

3.1 Comparison between TanSat and OCO-2 SIF Measurements

Directly comparing OCO-2 and TanSat SIF measurements could provide information on joint data application at the sounding scale for further studies. However, an identical sounding overlap barely exists because the two satellites often have different nadir tracks on the ground, which is induced by the different temporal and spatial intervals of the two satellite missions. Fortunately, the ground tracks of the two satellites were relatively close from April 17 to April 23, 2017. A couple of overlapping orbits were found in the measurements obtained from Africa with the orbit number of 1733 from TanSat and 14890a from OCO-2 (Figure 3). In the comparison, the OCO2_Level 2_Lite_SIF.8r product was used to present the SIF emission over the study area. These overlapping measurements encompassed multiple land cover types, in which the SIF varied within an acceptable time difference (<5 min).

Overall, measurements from the two satellites indicated SIF variation with land cover type. The SIF emission over evergreen broadleaf forests was larger than that over savannas, and grasslands exhibited the lowest SIF emission in April (Figure 3a,b). The mean SIF emission over evergreen broadleaf forests was approximately 0.9-1.1 W m^{-2} μm^{-1} sr^{-1}, whereas those over savannas and grasslands were 0.5-0.7 W m^{-2} μm^{-1} sr^{-1} and less than 0.1 W m^{-2} μm^{-1} sr^{-1}, respectively (Figure 3c,d). Furthermore, we also found a significant difference in the SIF emission intensity over tropical savannas, which was observed by both satellites (Figure 3c,d).

234
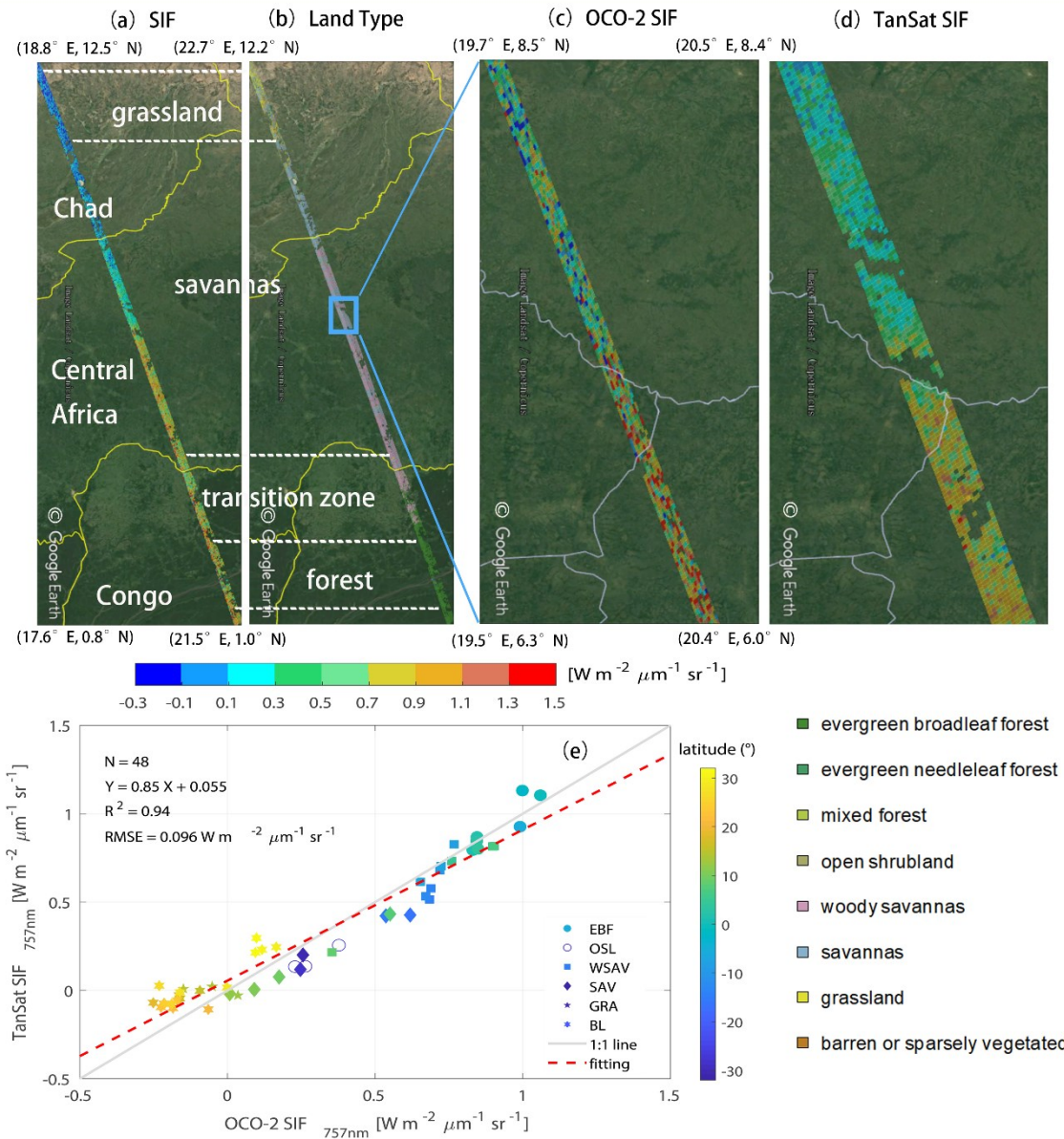
Figure 3: Overlapping orbits of TanSat and OCO-2 on April 19, 2017 over Africa displayed in Google Earth, (a) the SIF measurements from both the two satellites and (b) the footprint land cover type were compared. Compared to OCO-2, TanSat has a wider swath width. A zoom-in view over savannas shows variations in the SIF signal measured by (c) OCO-2 and (d) TanSat. The land surface image shown in Google earth is provided by Landsat/Copernicus team. Following the International Geosphere-Biosphere Programme classification scheme, the vertical legend on the bottom right corner depicts the land cover type that occurs in the study area. The middle horizontal color bar represents the intensity of the SIF radiance. (e) Small-area SIF comparison between OCO-2 and TanSat; each data point represents the mean SIF of a degree in latitude (colors) along the track. The marker legend that is shown on the bottom right of the plot indicates the dominant land cover (defined as the majority land cover type of each sounding) in each small area. There are six land cover types including evergreen broadleaf forest (EBF), open shrubland (OSL), woody savanna (WSAV), savanna (SAV), grassland (GRA), and barren land (BL). The red dashed line represents the linear fit between the two SIF products with statistics shown in the upper left of the plot. The gray line indicates a 1:1 relationship for reference.

247

248 Because the footprint sizes of the two satellites are different, it is difficult to make a direct footprint-to-footprint comparison.

249 Therefore, we made the comparison between the two satellite measurements based on a small area average. Each small area

250 spans a degree in latitude and continues along the track. The small area-averaged SIF comparison is shown in Figure 3e. The

251 results indicate good agreement, with an R^2 of 0.94 and an RMSE of 0.096 W m^{-2} μm^{-1} sr^{-1}. Additional ground-based SIF

252 measurement setups (Guanter et al., 2007; Liu et al., 2019; van der Tol et al., 2016; Yang et al., 2015a; Yu et al., 2019)

253 should allow for direct evaluation of satellite retrieval accuracy in the future.

254
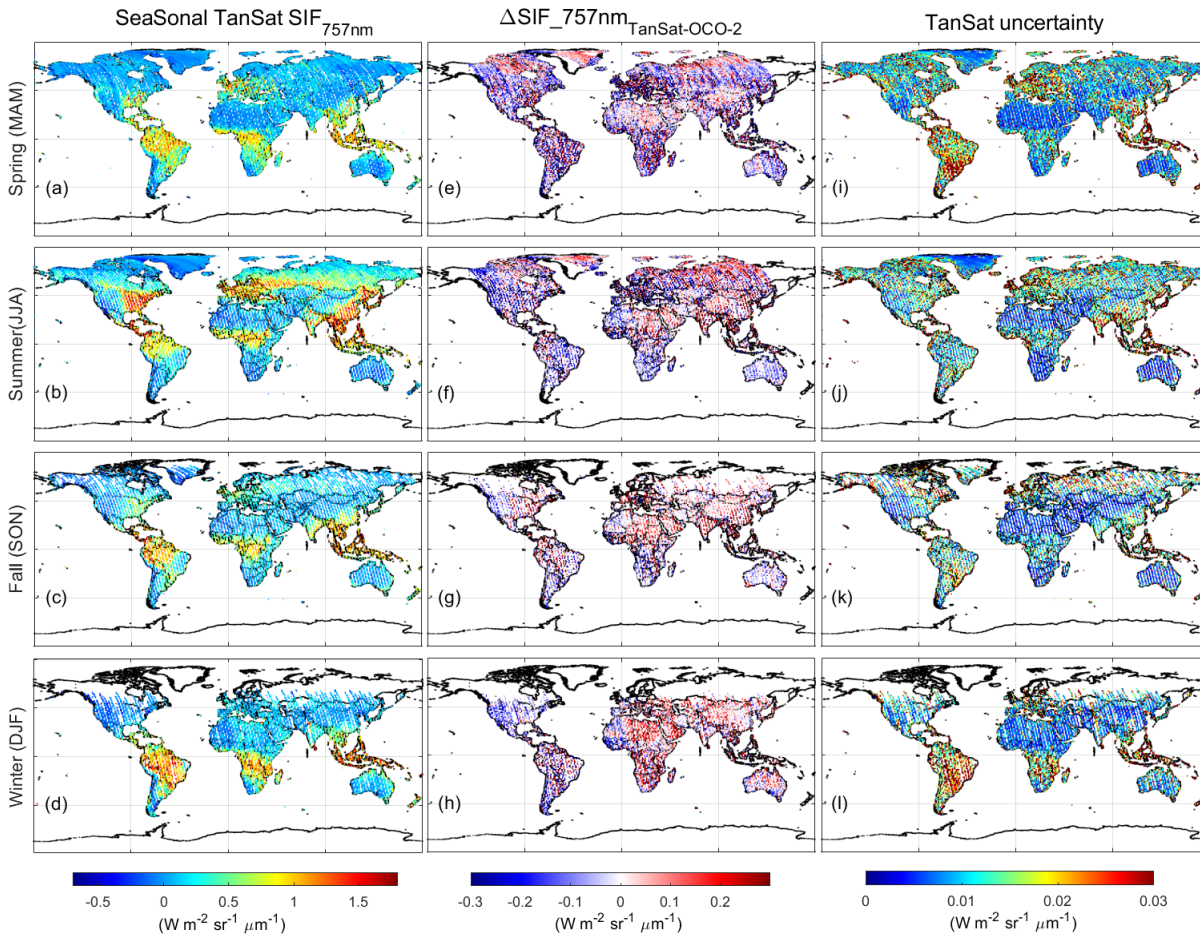
255

256 **Figure 4: Global TanSat SIF (left, a-d), differences between TanSat and IAPCAS OCO-2 SIF values (middle, e-h), and the grid-**
257 **cell retrieval uncertainty estimated from TanSat (right, i-l) at 1° × 1° spatial resolution. The maps in each row represent a**
258 **Northern Hemisphere season, i.e., spring (MAM), summer (JJA), fall (SON), and winter (DJF).**

259

260 Figure 4 shows the global SIF comparison between IAPCAS/SIF retrieved OCO-2 and TanSat; this comparison is only

261 performed at 1° × 1° spatial resolution. In general, the difference in SIF globally is mostly less than 0.3 W m^{-2} μm^{-1} sr^{-1} for

262 all seasons, and on average, the smallest difference appears in fall. There are regional biases observed in North Africa, South

263 Africa, South America, and Europe in all seasons except fall. This is mainly caused by the differences in instrument

264 performance between TanSat and OCO-2, such as the Instrument Respond Function and the Signal-to-Noise. The instrument

265 performance difference is represented by the different structural characteristics of the bias curves. The bias correction

266 compensates for most of the bias caused by instrument performance; however, small biases could remain. Furthermore, the

267 hundreds of kilometers of distance between the OCO-2 and TanSat footprints, for example, over different vegetation regions,

268 will also cause some measurement discrepancies. The global distribution of the two satellites was also compared with the

269 official OCO-2 SIF data on the global scale, the results show that the difference between the retrieved SIF maps and the

270 official map is less than 0.2 W m^{-2} μm^{-1} sr^{-1}, indicating that the retrieved SIF data from OCO-2 and TanSat both have good

271 SIF characterization capabilities on a global scale. The uncertainty σ of each sounding was estimated to validate SIF

272 reliability and is provided in the product. σ is derived from the retrieval error covariance matrix, $S_e = (K^T S_0^{-1} K)^{-1}$, where K

273 is the Jacobian matrix from the forward model fitting and S_0 is the measurement error covariance matrix that is calculated

274 from the instrument spectrum noise. In general, σ ranges from 0.1 to 0.6 W m^{-2} μm^{-1} sr^{-1} for both TanSat and OCO-2

275 measurements in the 757 nm fitting window, which is of a similar magnitude and data range as those of previous studies (Du

276 et al., 2018; Frankenberg et al., 2014a). Meanwhile, the standard error of the mean SIF in each grid σ_{meas} was estimated to

277 represent the gridded retrieval error and natural variability, which is calculated from TanSat SIF values with $\sigma_{meas} = \frac{\sigma_{std}}{\sqrt{n}}$

278 and $\sigma_{std} = \sqrt{\frac{\sum_{i=1}^{n}(SIF_i - \overline{SIF})^2}{n}}$, where σ_{std} represents the standard deviation of the grid cell with n soundings, SIF_i is the

279 retrieved SIF values of each sounding, and $\overline{SIF}$ is the mean SIF value for all measurements in the grid. As depicted in the

280 right column of Figure 4, the σ_{meas} of each grid cell is much lower than the precision of a single sounding. The σ_{meas} for

281 South America is larger than that for any other region on the globe (Figure 4i-l). This is similar to that of OCO-2 SIF

282 retrieval and caused by fewer effective measurements due to the South Atlantic Anomaly (Sun et al., 2018). The difference

283 in SIF emission values between the two satellites indicates that the collaborative usage of two satellite SIF products still

284 requires analysis of the impact of instrument differences, although the two satellite SIF products share the same

285 spatiotemporal pattern on a global scale.

3.2 SIF Global Distribution and Temporal Variation

287 The SIF emission intensity reflects the growth status of vegetation due to its correlation with photosynthetic efficiency;

288 hence, the overall global vegetation status can be represented by global SIF maps for each season. TanSat SIF over a whole

289 year's cycle, from March 2017 to February 2018, is represented seasonally as a 1° × 1° grid spatially. The seasonal variation

290 in SIF emission is clear in the Northern Hemisphere, i.e., it is enhanced from spring to summer and then decreases (Sun et al.,

291 2018).

292 In general, the SIF emission varied with latitude and the vegetation-covered areas near the equator maintained a continuous

293 SIF emission throughout the year. Large SIF emissions in the Northern Hemisphere, above 1.5 W m^{-2} μm^{-1} sr^{-1}, mostly from

294 the eastern U.S., southeast of China, and southern Asia in summer, were due to the large areas of cropland. There was also

295 an obvious SIF emission of 1-1.2 W m^{-2} μm^{-1} sr^{-1} observed over Central Europe and northeastern China during the summer.

296 In these regions, croplands and deciduous forests contribute to SIF emissions. In the Southern Hemisphere, the strongest SIF

297 emission occurred in the Amazon, with a level of approximately 1-2 W m^{-2} μm^{-1} sr^{-1} in DJF (Northern Hemisphere winter),

298 where there is an evergreen broadleaf rainforest. Africa, which is covered by evergreen broadleaf rainforests and woody

299 savannas, had an average SIF value of 0.7-1.5 W m^{-2} μm^{-1} sr^{-1} during the year.

300 The SIF-GPP relationship over different vegetation types was also investigated by comparing the annual mean satellite SIF

301 measurements with the FLUXCOM GPP (Jung et al., 2020; Tramontana et al., 2016) dataset in a 1° × 1° grid over the globe.

302 The FLUXCOM GPP dataset used in the study comprises monthly global gridded flux products with remote sensing and

303 meteorological/climate forcing (RS+METEO) setups, which are derived from mean seasonal cycles according to MODIS

304 data and daily meteorological information (Jung et al., 2020; Tramontana et al., 2016). The satellite-measured SIF is an

305 instantaneous emission signal that varies with incident solar radiance within the day. To reduce the differences caused by the

306 observation time and SZA at different latitudes, we applied a daily adjustment factor to convert the instantaneous SIF

307 emission into a daily mean SIF (Du et al., 2018; Frankenberg et al., 2011b; Sun et al., 2018). The daily adjustment factor d is

308 calculated as follows:

309
$$d = \frac{\int_{t=t_0-12h}^{t=t_0+12h} cos\,(SZA(t))\cdot dt}{cos(SZA(t_0))} \tag{5}$$

310 where t_0 is the observation time in fractional days and $SZA(t)$ is a function of latitude, longitude, and time for calculating

311 the SZA of the measurements. The annual averaged SIF is calculated from the daily mean SIF. To evaluate the relationship

312 between SIF and GPP on the periodic scale of vegetation growth status, annually-averaged data were used in the regression

313 fitting analysis.

314
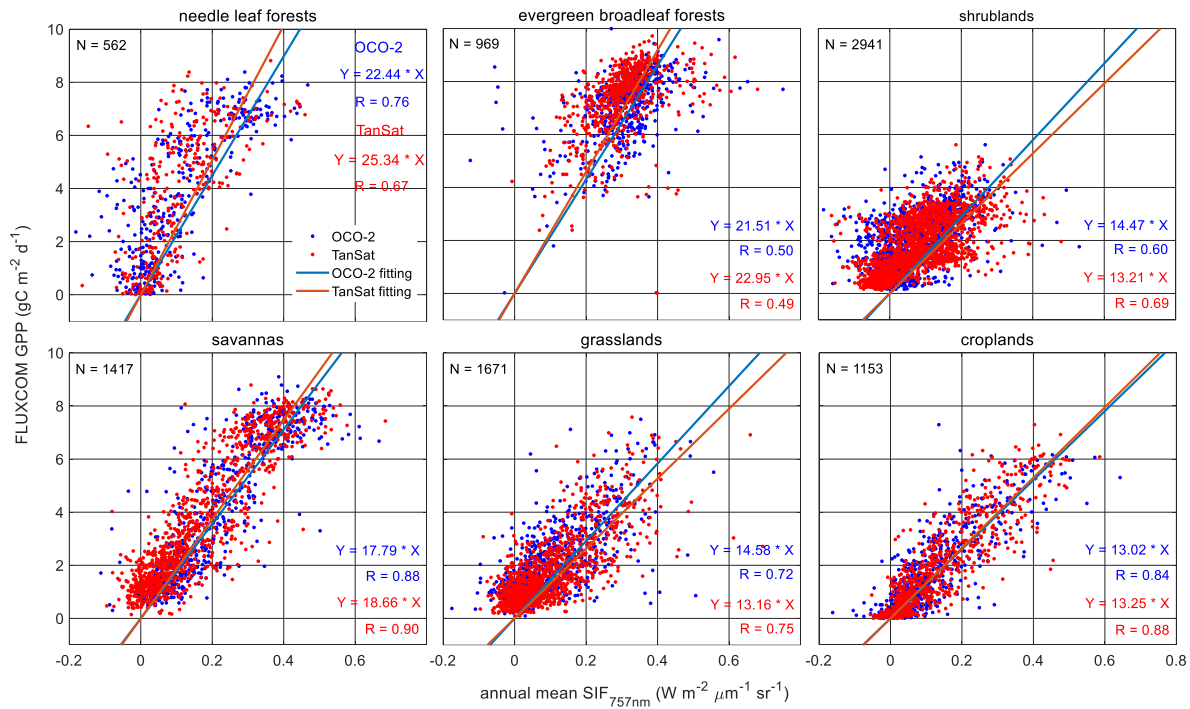
Figure 5: Relationship between annual mean SIF and FLUXCOM gross primary production (GPP) from March 2017 to February 2018. Blue and red dots represent OCO-2 and TanSat SIF grids, respectively. Fitted lines and statistics for OCO-2 and TanSat are shown in each plot.

Figure 5 shows the linear fits for six vegetation types, including needle leaf forest, evergreen broadleaf forest, shrubland, savanna, grassland, and cropland. Recent studies have shown a strong linear correlation between SIF and GPP. The TanSat SIF and the OCO-2 official SIF data were used to estimation the SIF-GPP correlation. To make a direct comparison of the relationship between SIF and GPP among various vegetation types, we used non-offset linear fitting to indicate the correlation between satellite SIF and FLUXCOM GPP. For savanna and cropland, there were strong relationships between the mean SIF and GPP with an R-value above 0.84. The fitting results show that the SIF products of the two satellites have similar capabilities in characterizing GPP, especially for the evergreen broadleaf forest, savanna, and cropland, with slopes of approximately 21, 18, and 13, respectively. For shrubland and grassland, the slope of OCO-2 SIF with GPP is higher than that of TanSat and has a worse correlation. For forests, OCO-2 SIF present a better correlation with GPP, especially in the needle leaf forest. The markedly different fitting slopes across various biomes suggest that the application of SIF in GPP estimation needs more detailed analysis although the evidence of the strong linear relationship between them.

4 Conclusions

In this paper, we introduced the retrieval algorithm IAPCAS/SIF and its application in TanSat and OCO-2 measurements. One-year (March 2017-February 2018) TanSat SIF data was introduced and compared with OCO-2 measurements in this

study. The TanSat and OCO-2 SIF products based on the IAPCAS/SIF algorithm are available on the Cooperation on the Analysis of carbon SAtellites data (CASA) website, www.chinageoss.org/tansat. Comparisons between TanSat and OCO-2 measurements directly, using a case study, and indirectly, with global 1°×1° grid data, showed consistency between the two satellite missions, indicating that the coordinated usage of the two data products is possible in future studies. With increasing satellites becoming available for SIF observations, space-based SIF observations have recently expanded in range to provide broad spatiotemporal coverage. The next-generation Chinese carbon monitoring satellite (TanSat-2) is now in the preliminary design phase, which is designed to be a constellation of six satellites to measure different kinds of greenhouse gases and trace gases in a more efficient way, including CO_2, CH_4, CO, NOx, as well as SIF. SIF measurements from TanSat-2 will provide global data products over broader coverage areas with less noise. The improvement in the spatiotemporal resolution of SIF data will benefit GPP predictions based on the numerous studies of the linear relationship between SIF and GPP. In future work, the measurement accuracy should be validated directly using ground-based measurements to ensure data quality.

Data availability

The SIF products of TanSat and OCO-2 by IAPCAS/SIF algorithm are available on the Cooperation on the Analysis of carbon SAtellites data (CASA) website (www.chinageoss.org/tansat).

Author contributions

L.Y. and D.Y. developed the retrieval algorithm, designed the study, and wrote the paper. Y.L. led the SIF data process and analysis. Y.L., D.Y., Z.C., and J.W. contributed to manuscript organization and revision. C.L. and Y.Z. provided information on the TanSat instrument performance. L.T. provided TanSat in-flight information. M.W. and S.W. provided information on the scientific requirement for data further application. N.L. and D.L. led the TanSat data application. Z.Y. led the TanSat in-flight operation.

Competing interests

The authors declare that they have no conflict of interest.

Acknowledgments

The TanSat L1B data service was provided by the International Reanalysis Cooperation on Carbon Satellites Data (IRCSD) and the Cooperation on the Analysis of carbon SAtellites data (CASA). The authors thank OCO-2 Team for providing

Level-1B data and Level-2 SIF data products. The authors thank the FLUXCOM team for providing global GPP data. The authors thank Google for allowing free use of Google Earth and reproduction of maps for publication. The authors also thank the Landsat/Copernicus team for providing land surface images for Google Earth.

Financial support

This work has been supported by the Key Research Program of the Chinese Academy of Sciences (ZDRW-ZS-2019-1), and the Youth Program of the National Natural Science Foundation of China (41905029).

References

Boesche, E., Stammes, P., and Bennartz, R.: Aerosol influence on polarization and intensity in near-infrared O_2 and CO_2 absorption bands observed from space, J. Quant. Spectrosc. Radiat. Transf., 110, 223–239, https://doi.org/10.1016/j.jqsrt.2008.09.019, 2009.

Butz, A., Guerlet, S., Hasekamp, O., Schepers, D., Galli, A., Aben, I., Frankenberg, C., Hartmann, J. M., Tran, H., Kuze, A., Keppel-Aleks, G., Toon, G., Wunch, D., Wennberg, P., Deutscher, N., Griffith, D., MacAtangay, R., Messerschmidt, J., Notholt, J., and Warneke, T.: Toward accurate CO_2 and CH_4 observations from GOSAT, Geophys. Res. Lett., 38, 2–7, https://doi.org/10.1029/2011GL047888, 2011.

Butz, A., Hasekamp, O. P., Frankenberg, C., and Aben, U.: Retrievals of atmospheric CO_2 from simulated space-borne measurements of backscattered near-infrared sunlight: Accounting for aerosol effects, Appl. Opt., 48, 3322–3336, https://doi.org/10.1364/AO.48.003322, 2009.

Butz, A., Hasekamp, O. P., Frankenberg, C., Vidot, J., and Aben, I.: CH_4 retrievals from space-based solar backscatter measurements: Performance evaluation against simulated aerosol and cirrus loaded scenes, J. Geophys. Res. Atmos., 115, 1–15, https://doi.org/10.1029/2010JD014514, 2010.

Cai, Z. N., Liu, Y., and Yang, D. X.: Analysis of XCO2 retrieval sensitivity using simulated Chinese Carbon Satellite (TanSat) measurements, Sci. China Earth Sci., 57, 1919–1928, https://doi.org/10.1007/s11430-013-4707-1, 2014.

Chen, A., Mao, J., Ricciuto, D., Xiao, J., Frankenberg, C., Li, X., Thornton, P. E., Gu, L., and Knapp, A. K.: Moisture availability mediates the relationship between terrestrial gross primary production and solar-induced chlorophyll fluorescence: Insights from global-scale variations, Glob. Chang. Biol., 1–13, https://doi.org/10.1111/gcb.15373, 2020.

Doughty, R., Köhler, P., Frankenberg, C., Magney, T. S., Xiao, X., Qin, Y., Wu, X., and Moore, B.: TROPOMI reveals dry-season increase of solar-induced chlorophyll fluorescence in the Amazon forest, Proc. Natl. Acad. Sci. U. S. A., 116, 22393–22398, https://doi.org/10.1073/pnas.1908157116, 2019.

387   Drusch, M., Moreno, J., del Bello, U., Franco, R., Goulas, Y., Huth, A., Kraft, S., Middleton, E. M., Miglietta, F.,

388   Mohammed, G.: The FLuorescence EXplorer Mission Concept—ESA's Earth Explorer 8, ITGRS, 55, 1273–1284,

389   http://doi.org./10.1109/TGRS.2016.2621820, 2017.

390   Du, S., Liu, L., Liu, X., Zhang, X., Zhang, X., Bi, Y., and Zhang, L.: Retrieval of global terrestrial solar-induced chlorophyll

391   fluorescence from TanSat satellite, Sci. Bull., 63, 1502–1512, https://doi.org/10.1016/j.scib.2018.10.003, 2018.

392   Frankenberg, C., Butz, A., and Toon, G. C.: Disentangling chlorophyll fluorescence from atmospheric scattering effects in

393   O_2 A-band spectra of reflected sunlight, Geophys. Res. Lett., 38, 1–5, https://doi.org/10.1029/2010GL045896, 2011a.

394   Frankenberg, C., Fisher, J. B., Worden, J., Badgley, G., Saatchi, S. S., Lee, J. E., Toon, G. C., Butz, A., Jung, M., Kuze, A.,

395   and Yokota, T.: New global observations of the terrestrial carbon cycle from GOSAT: Patterns of plant fluorescence with

396   gross primary productivity, Geophys. Res. Lett., 38, 1–6, https://doi.org/10.1029/2011GL048738, 2011b.

397   Frankenberg, C., O'Dell, C., Berry, J., Guanter, L., Joiner, J., Köhler, P., Pollock, R., and Taylor, T. E.: Prospects for

398   chlorophyll fluorescence remote sensing from the Orbiting Carbon Observatory-2, Remote Sens. Environ., 147, 1–12,

399   https://doi.org/10.1016/j.rse.2014.02.007, 2014a.

400   Frankenberg, C., O'Dell, C., Guanter, L., and McDuffie, J.: Remote sensing of near-infrared chlorophyll fluorescence from

401   space in scattering atmospheres: Implications for its retrieval and interferences with atmospheric CO_2 retrievals, Atmos.

402   Meas. Tech., 5, 2081–2094, https://doi.org/10.5194/amt-5-2081-2012, 2012.

403   Frankenberg, C.: OCO-2 Algorithm Theoretical Basis Document: IMAP-DOAS pre-processor, 2014b.

404   Guanter, L., Aben, I., Tol, P., Krijger, J. M., Hollstein, A., Köhler, P., Damm, A., Joiner, J., Frankenberg, C., and Landgraf,

405   J.: Potential of the TROPOspheric Monitoring Instrument (TROPOMI) onboard the Sentinel-5 Precursor for the monitoring

406   of terrestrial chlorophyll fluorescence, https://doi.org/10.5194/amt-8-1337-2015, 2015.

407   Guanter, L., Alonso, L., Gómez-Chova, L., Amorós-López, J., Vila, J., and Moreno, J.: Estimation of solar-induced

408   vegetation fluorescence from space measurements, Geophys. Res. Lett., 34, 1–5, https://doi.org/10.1029/2007GL029289,

409   2007.

410   Guanter, L., Frankenberg, C., Dudhia, A., Lewis, P. E., Gómez-Dans, J., Kuze, A., Suto, H., and Grainger, R. G.: Retrieval

411   and global assessment of terrestrial chlorophyll fluorescence from GOSAT space measurements, Remote Sens. Environ., 121,

412   236–251, https://doi.org/10.1016/j.rse.2012.02.006, 2012.

413   Guanter, L., Zhang, Y., Jung, M., Joiner, J., Voigt, M., Berry, J. A., Frankenberg, C., Huete, A. R., Zarco-Tejada, P., Lee, J.

414   E., Moran, M. S., Ponce-Campos, G., Beer, C., Camps-Valls, G., Buchmann, N., Gianelle, D., Klumpp, K., Cescatti, A.,

415   Baker, J. M., and Griffis, T. J.: Global and time-resolved monitoring of crop photosynthesis with chlorophyll fluorescence,

416   Proc. Natl. Acad. Sci. U. S. A., 111, https://doi.org/10.1073/pnas.1320008111, 2014.

417   Joiner, J., Guanter, L., Lindstrot, R., Voigt, M., Vasilkov, A. P., Middleton, E. M., Huemmrich, K. F., Yoshida, Y., and

418   Frankenberg, C.: Global monitoring of terrestrial chlorophyll fluorescence from moderate-spectral-resolution near-infrared

419   satellite measurements: methodology, simulations, and application to GOME-2, Atmos. Meas. Tech., 6, 2803–2823,

420   https://doi.org/10.5194/amt-6-2803-2013, 2013.

421 Joiner, J., Yoshida, Y., Guanter, L., and Middleton, E. M.: New methods for the retrieval of chlorophyll red fluorescence
422 from hyperspectral satellite instruments: simulations and application to GOME-2 and SCIAMACHY, Atmos. Meas. Tech., 9,
423 3939–3967, https://doi.org/10.5194/amt-9-3939-2016, 2016.

424 Joiner, J., Yoshida, Y., Vasilkov, A. P., Middleton, E. M., Campbell, P. K. E., Yoshida, Y., Kuze, A., and Corp, L. A.:
425 Filling-in of near-infrared solar lines by terrestrial fluorescence and other geophysical effects: simulations and space-based
426 observations from SCIAMACHY and GOSAT, Atmos. Meas. Tech., 5, 809–829, https://doi.org/10.5194/amt-5-809-2012,
427 2012.

428 Joiner, J., Yoshida, Y., Vasilkov, A. P., Yoshida, Y., Corp, L. A., and Middleton, E. M.: First observations of global and
429 seasonal terrestrial chlorophyll fluorescence from space, 8, 637–651, https://doi.org/10.5194/bg-8-637-2011, 2011.

430 Joiner, J., Yoshida, Y., Zhang, Y., Duveiller, G., Jung, M., Lyapustin, A., Wang, Y., and Tucker, C. J.: Estimation of
431 terrestrial global gross primary production (GPP) with satellite data-driven models and eddy covariance flux data, Remote
432 Sens., 10, 1–38, https://doi.org/10.3390/rs10091346, 2018.

433 Jung, M., Schwalm, C., Migliavacca, M., Walther, S., Camps-Valls, G., Koirala, S., Anthoni, P., Besnard, S., Bodesheim, P.,
434 Carvalhais, N., Chevallier, F., Gans, F., S Goll, D., Haverd, V., Köhler, P., Ichii, K., K Jain, A., Liu, J., Lombardozzi, D., E
435 M S Nabel, J., A Nelson, J., O'Sullivan, M., Pallandt, M., Papale, D., Peters, W., Pongratz, J., Rödenbeck, C., Sitch, S.,
436 Tramontana, G., Walker, A., Weber, U., and Reichstein, M.: Scaling carbon fluxes from eddy covariance sites to globe:
437 Synthesis and evaluation of the FLUXCOM approach, 17, 1343–1365, https://doi.org/10.5194/bg-17-1343-2020, 2020.

438 Köhler, P., Frankenberg, C., Magney, T. S., Guanter, L., Joiner, J., and Landgraf, J.: Global Retrievals of Solar-Induced
439 Chlorophyll Fluorescence With TROPOMI: First Results and Intersensor Comparison to OCO-2, Geophys. Res. Lett., 45,
440 10,456-10,463, https://doi.org/10.1029/2018GL079031, 2018b.

441 Köhler, P., Guanter, L., and Joiner, J.: A linear method for the retrieval of sun-induced chlorophyll fluorescence from
442 GOME-2 and SCIAMACHY data, Atmos. Meas. Tech., 8, 2589–2608, https://doi.org/10.5194/amt-8-2589-2015, 2015.

443 Köhler, P., Guanter, L., Kobayashi, H., Walther, S., and Yang, W.: Assessing the potential of sun-induced fluorescence and
444 the canopy scattering coefficient to track large-scale vegetation dynamics in Amazon forests, Remote Sens. Environ., 204,
445 769–785, https://doi.org/10.1016/j.rse.2017.09.025, 2018a.

446 Lee, J. E., Frankenberg, C., Van Der Tol, C., Berry, J. A., Guanter, L., Boyce, C. K., Fisher, J. B., Morrow, E., Worden, J. R.,
447 Asefi, S., Badgley, G., and Saatchi, S.: Forest productivity and water stress in Amazonia: Observations from GOSAT
448 chlorophyll fluorescence, Tohoku J. Exp. Med., 230, https://doi.org/10.1098/rspb.2013.0171, 2013.

449 Li, X., Xiao, J., and He, B.: Chlorophyll fluorescence observed by OCO-2 is strongly related to gross primary productivity
450 estimated from flux towers in temperate forests, Remote Sens. Environ., 204, 659–671,
451 https://doi.org/10.1016/j.rse.2017.09.034, 2018.

452 Li, X., Xiao, J., Kimball, J. S., Reichle, R. H., Scott, R. L., Litvak, M. E., Bohrer, G., and Frankenberg, C.: Synergistic use of
453 SMAP and OCO-2 data in assessing the responses of ecosystem productivity to the 2018 U.S. drought, Remote Sens.
454 Environ., 251, 112062, https://doi.org/10.1016/j.rse.2020.112062, 2020.

Liu, X., Guanter, L., Liu, L., Damm, A., Malenovský, Z., Rascher, U., Peng, D., Du, S., and Gastellu-Etchegorry, J. P.: Downscaling of solar-induced chlorophyll fluorescence from canopy level to photosystem level using a random forest model, Remote Sens. Environ., 231, 110772, https://doi.org/10.1016/j.rse.2018.05.035, 2019.

Liu, Y., Wang, J., Yao, L., Chen, X., Cai, Z., Yang, D., Yin, Z., Gu, S., Tian, L., Lu, N., and Lyu, D.: The TanSat mission: preliminary global observations, Sci. Bull., 63, 1200–1207, https://doi.org/10.1016/j.scib.2018.08.004, 2018.

MacBean, N., Maignan, F., Bacour, C., Lewis, P., Peylin, P., Guanter, L., Köhler, P., Gómez-Dans, J., and Disney, M.: Strong constraint on modelled global carbon uptake using solar-induced chlorophyll fluorescence data, Sci. Rep., 8, 1–12, https://doi.org/10.1038/s41598-018-20024-w, 2018.

O'Dell, C. W., Connor, B., Bösch, H., O'Brien, D., Frankenberg, C., Castano, R., Christi, M., Eldering, D., Fisher, B., Gunson, M., McDuffie, J., Miller, C. E., Natraj, V., Oyafuso, F., Polonsky, I., Smyth, M., Taylor, T., Toon, G. C., Wennberg, P. O., and Wunch, D.: The ACOS CO2 retrieval algorithm-Part 1: Description and validation against synthetic observations, Atmos. Meas. Tech., 5, 99–121, https://doi.org/10.5194/amt-5-99-2012, 2012.

Qiu, R., Han, G., Ma, X., Xu, H., Shi, T., and Zhang, M.: A comparison of OCO-2 SIF, MODIS GPP, and GOSIF data from gross primary production (GPP) estimation and seasonal cycles in North America, Remote Sens., 12, https://doi.org/10.3390/rs12020258, 2020.

Reuter, M., Buchwitz, M., Schneising, O., Heymann, J., Bovensmann, H., and Burrows, J. P.: A method for improved SCIAMACHY CO_2 retrieval in the presence of optically thin clouds, Atmos. Meas. Tech., 3, 209–232, https://doi.org/10.5194/amt-3-209-2010, 2010.

Sun, K., Liu, X., Nowlan, C. R., Cai, Z., Chance, K., Frankenberg, C., Lee, R. A. M., Pollock, R., Rosenberg, R., and Crisp, D.: Characterization of the OCO-2 instrument line shape functions using on-orbit solar measurements, Atmos. Meas. Tech., 10, 939–953, https://doi.org/10.5194/amt-10-939-2017, 2017b.

Sun, Y., Frankenberg, C., Jung, M., Joiner, J., Guanter, L., Köhler, P., and Magney, T.: Overview of Solar-Induced chlorophyll Fluorescence (SIF) from the Orbiting Carbon Observatory-2: Retrieval, cross-mission comparison, and global monitoring for GPP, Remote Sens. Environ., 209, 808–823, https://doi.org/10.1016/j.rse.2018.02.016, 2018.

Sun, Y., Frankenberg, C., Wood, J. D., Schimel, D. S., Jung, M., Guanter, L., Drewry, D. T., Verma, M., Porcar-Castell, A., Griffis, T. J., Gu, L., Magney, T. S., Köhler, P., Evans, B., and Yuen, K.: OCO-2 advances photosynthesis observation from space via solar-induced chlorophyll fluorescence, Science (80-.)., 358, https://doi.org/10.1126/science.aam5747, 2017a.

Sun, Y., Fu, R., Dickinson, R., Joiner, J., Frankenberg, C., Gu, L., Xia, Y., and Fernando, N.: Drought onset mechanisms revealed by satellite solar-induced chlorophyll fluorescence: Insights from two contrasting extreme events, J. Geophys. Res. G Biogeosciences, 120, 2427–2440, https://doi.org/10.1002/2015JG003150, 2015.

Tramontana, G., Jung, M., Schwalm, C. R., Ichii, K., Camps-Valls, G., Ráduly, B., Reichstein, M., Arain, M. A., Cescatti, A., Kiely, G., Merbold, L., Serrano-Ortiz, P., Sickert, S., Wolf, S., and Papale, D.: Predicting carbon dioxide and energy fluxes across global FLUXNET sites with regression algorithms, 13, 4291–4313, https://doi.org/10.5194/bg-13-4291-2016, 2016.

van der Tol, C., Rossini, M., Cogliati, S., Verhoef, W., Colombo, R., Rascher, U., and Mohammed, G.: A model and measurement comparison of diurnal cycles of sun-induced chlorophyll fluorescence of crops, Remote Sens. Environ., 186, 663–677, https://doi.org/10.1016/j.rse.2016.09.021, 2016.

Yang, D., Boesch, H., Liu, Y., Somkuti, P., Cai, Z., Chen, X., Di Noia, A., Lin, C., Lu, N., Lyu, D., Parker, R. J., Tian, L., Wang, M., Webb, A., Yao, L., Yin, Z., Zheng, Y., Deutscher, N. M., Griffith, D. W. T., Hase, F., Kivi, R., Morino, I., Notholt, J., Ohyama, H., Pollard, D. F., Shiomi, K., Sussmann, R., Té, Y., Velazco, V. A., Warneke, T., and Wunch, D.: Toward High Precision XCO2 Retrievals From TanSat Observations: Retrieval Improvement and Validation Against TCCON Measurements, J. Geophys. Res. Atmos., 125, 1–26, https://doi.org/10.1029/2020JD032794, 2020.

Yang, D., Liu, Y., Boesch, H., Yao, L., Di Noia, A., Cai, Z., Lu, N., Lyu, D., Wang, M., Wang, J., Yin, Z., and Zheng, Y.: A New TanSat XCO2 Global Product towards Climate Studies, Adv. Atmos. Sci., 38, 8–11, https://doi.org/10.1007/s00376-020-0297-y, 2021.

Yang, D., Liu, Y., Cai, Z., Chen, X., Yao, L., and Lu, D.: First Global Carbon Dioxide Maps Produced from TanSat Measurements, Adv. Atmos. Sci., 35, 621–623, https://doi.org/10.1007/s00376-018-7312-6, 2018.

Yang, D., Liu, Y., Cai, Z., Deng, J., Wang, J., and Chen, X.: An advanced carbon dioxide retrieval algorithm for satellite measurements and its application to GOSAT observations, Sci. Bull., 60, 2063–2066, https://doi.org/10.1007/s11434-015-0953-2, 2015b.

Yang, X., Tang, J., Mustard, J. F., Lee, J. E., Rossini, M., Joiner, J., Munger, J. W., Kornfeld, A., and Richardson, A. D.: Solar-induced chlorophyll fluorescence that correlates with canopy photosynthesis on diurnal and seasonal scales in a temperate deciduous forest, Geophys. Res. Lett., 42, 2977–2987, https://doi.org/10.1002/2015GL063201, 2015a.

Yao, L., Yang, D., Liu, Y., Wang, J., Liu, L., Du, S., Cai, Z., Lu, N., Lyu, D., Wang, M., Yin, Z., and Zheng, Y.: A New Global Solar-induced Chlorophyll Fluorescence (SIF) Data Product from TanSat Measurements, Adv. Atmos. Sci., 38, 341–345, https://doi.org/10.1007/s00376-020-0204-6, 2021.

Yin, Y., Byrne, B., Liu, J., Wennberg, P. O., Davis, K. J., Magney, T., Köhler, P., He, L., Jeyaram, R., Humphrey, V., Gerken, T., Feng, S., Digangi, J. P., and Frankenberg, C.: Cropland Carbon Uptake Delayed and Reduced by 2019 Midwest Floods, AGU Adv., 1, 1–15, https://doi.org/10.1029/2019av000140, 2020.

Yoshida, Y., Joiner, J., Tucker, C., Berry, J., Lee, J. E., Walker, G., Reichle, R., Koster, R., Lyapustin, A., and Wang, Y.: The 2010 Russian drought impact on satellite measurements of solar-induced chlorophyll fluorescence: Insights from modeling and comparisons with parameters derived from satellite reflectances, Remote Sens. Environ., 166, 163–177, https://doi.org/10.1016/j.rse.2015.06.008, 2015.

Yoshida, Y., Kikuchi, N., Morino, I., Uchino, O., Oshchepkov, S., Bril, A., Saeki, T., Schutgens, N., Toon, G. C., Wunch, D., Roehl, C. M., Wennberg, P. O., Griffith, D. W. T., Deutscher, N. M., Warneke, T., Notholt, J., Robinson, J., Sherlock, V., Connor, B., Rettinger, M., Sussmann, R., Ahonen, P., Heikkinen, P., Kyrö, E., Mendonca, J., Strong, K., Hase, F., Dohe, S., and Yokota, T.: Improvement of the retrieval algorithm for GOSAT SWIR XCO2and XCH4and their validation using TCCON data, Atmos. Meas. Tech., 6, 1533–1547, https://doi.org/10.5194/amt-6-1533-2013, 2013.

522 Yoshida, Y., Ota, Y., Eguchi, N., Kikuchi, N., Nobuta, K., Tran, H., Morino, I., and Yokota, T.: Retrieval algorithm for CO_2
523 and CH_4 column abundances from short-wavelength infrared spectral observations by the Greenhouse gases observing
524 satellite, Atmos. Meas. Tech., 4, 717–734, https://doi.org/10.5194/amt-4-717-2011, 2011.

525 Yu, L., Wen, J., Chang, C. Y., Frankenberg, C., and Sun, Y.: High-Resolution Global Contiguous SIF of OCO-2, Geophys.
526 Res. Lett., 46, 1449–1458, https://doi.org/10.1029/2018GL081109, 2019.

527 Zhang, Y., Guanter, L., Berry, J. A., Joiner, J., van der Tol, C., Huete, A., Gitelson, A., Voigt, M., and Köhler, P.: Estimation
528 of vegetation photosynthetic capacity from space-based measurements of chlorophyll fluorescence for terrestrial biosphere
529 models, Glob. Chang. Biol., 20, 3727–3742, https://doi.org/10.1111/gcb.12664, 2014.

530 Zhang, Y., Xiao, X., Zhang, Y., Wolf, S., Zhou, S., Joiner, J., Guanter, L., Verma, M., Sun, Y., Yang, X., Paul-Limoges, E.,
531 Gough, C. M., Wohlfahrt, G., Gioli, B., van der Tol, C., Yann, N., Lund, M., and de Grandcourt, A.: On the relationship
532 between sub-daily instantaneous and daily total gross primary production: Implications for interpreting satellite-based SIF
533 retrievals, Remote Sens. Environ., 205, 276–289, https://doi.org/10.1016/j.rse.2017.12.009, 2018.

534

535

536

537